

## OBSERVATIONS AND NONLINEAR FORCE-FREE FIELD MODELING OF ACTIVE REGION 10953

YINGNA SU<sup>1,2</sup>, ADRIAAN VAN BALLEGOOIJEN<sup>1</sup>, BRUCE W. LITES<sup>3</sup>, EDWARD E. DELUCA<sup>1</sup>, LEON GOLUB<sup>1</sup>, PAOLO C. GRIGIS<sup>1</sup>,  
GUANGLI HUANG<sup>2</sup>, AND HAISHENG JI<sup>2</sup>

<sup>1</sup> Harvard-Smithsonian Center for Astrophysics, Cambridge, MA 02138, USA; ynsu@head.cfa.harvard.edu

<sup>2</sup> Purple Mountain Observatory, Nanjing, 210008, China

<sup>3</sup> High Altitude Observatory, P.O. Box 3000, Boulder, CO 80307-3000, USA

Received 2008 August 6; accepted 2008 September 22; published 2009 January 7

### ABSTRACT

We present multiwavelength observations of a simple bipolar active region (NOAA 10953), which produced several small flares (mostly B class and one C8.5 class) and filament activations from April 30 to May 3 in 2007. We also explore nonlinear force-free field (NLFFF) modeling of this region prior to the C8.5 flare on May 2, using magnetograph data from *SOHO*/MDI and *Hinode*/SOT. A series of NLFFF models are constructed using the flux-rope insertion method. By comparing the modeled field lines with multiple X-ray loops observed by *Hinode*/XRT, we find that the axial flux of the flux rope in the best-fit models is  $(7 \pm 2) \times 10^{20}$  Mx, while the poloidal flux has a wider range of  $(0.1\text{--}10) \times 10^{10}$  Mx cm<sup>-1</sup>. The axial flux in the best-fit model is well below the upper limit ( $\sim 15 \times 10^{20}$  Mx) for stable force-free configurations, which is consistent with the fact that no successful full filament eruption occurred in this active region. From multiwavelength observations of the C8.5 flare, we find that the X-ray brightenings (in both *RHESSI* and XRT) appeared about 20 minutes earlier than the EUV brightenings seen in TRACE 171 Å images and filament activations seen in MLSO H $\alpha$  images. This is interpreted as an indication that the X-ray emission may be caused by direct coronal heating due to reconnection, and the energy transported down to the chromosphere may be too low to produce EUV brightenings. This flare started from nearly unsheared flare loop, unlike most two-ribbon flares that begin with highly sheared footpoint brightenings. By comparing with our NLFFF model, we find that the early flare loop is located above the flux rope that has a sharp boundary. We suggest that this flare started near the outer edge of the flux rope, not at the inner side or at the bottom as in the standard two-ribbon flare model.

**Key words:** Sun: corona – Sun: filaments – Sun: flares – Sun: magnetic fields – Sun: photosphere – Sun: X-rays, gamma rays

*Online-only material:* color figure, mpeg animation

### 1. INTRODUCTION

It is well accepted that solar flares, prominence eruptions, and coronal mass ejections (CMEs) are different manifestations of a single physical process thought to be powered by the release of free energy stored in the corona prior to the activities. Storage of free energy requires a non-potential magnetic field, and it is therefore associated with a shear or twist in the coronal field away from the potential, current-free state (Priest & Forbes 2002). Twisted or sheared magnetic fields are often visible in the solar corona before solar eruptions (Rust & Kumar 1996; Canfield et al. 1999; Moore et al. 2001; Su et al. 2006, 2007a; 2007b, Ji et al. 2008), but it is unclear how the eruption gets started. To determine what triggers such eruptions and how the energy is released, we need to understand the three-dimensional (3D) structure of the coronal magnetic field configuration prior to the flare. Therefore, modeling of the preflare nonpotential fields is needed.

In this paper, we consider a C8.5 flare that occurred in Active Region (AR) 10953 on 2007 May 2, and we develop a model for the nonpotential fields before the flare. The evolution of the sheared magnetic field in this region was studied by Okamoto et al. (2008), using vector magnetograms from *Hinode*/SOT/SP. They suggested that the observed vector fields show the evidence for the emergence of a magnetic flux rope. The purpose of the current paper is to develop a 3D magnetic model of this flux rope, and to study where the flare occurs in relationship to the flux rope.

A realistic way to model the nonpotential coronal fields in active regions is to assume that the electric currents are parallel to the magnetic field,  $\nabla \times \vec{B} = \alpha \vec{B}$ , with  $\alpha$  being constant only along every field line ( $\vec{B} \cdot \nabla \alpha = 0$ ) but varying from field line to field line, giving us the nonlinear force-free field (NLFFF). Several authors have developed methods for reconstructing the NLFFFs by extrapolating observed photospheric vector fields into the corona (e.g., Mikić & McClymont 1994; Wheatland et al. 2000; Yan & Sakurai 2000; Bleybel et al. 2002; Régnier et al. 2002; Wheatland 2006; Wiegelmann 2004; Wiegelmann et al. 2006; Song et al. 2006). For reviews of these various methods, see Schrijver et al. (2006, 2008), Wiegelmann (2008), and Metcalf et al. (2008).

Measurements of photospheric vector magnetic fields and their use as boundary conditions in extrapolation are subject to a number of uncertainties (see McClymont et al. 1997). Most importantly, the magnetic field in the photosphere is not force free, and the highly sheared field in the filament channel is not always visible in the photosphere where the vector field measurements are made (Lites 2005). Therefore, in the present study we construct NLFFF models using the flux rope insertion method (van Ballegoijen 2004; van Ballegoijen & Mackay 2007), which uses observational constraints from coronal images in combination with photospheric magnetograms. The method only requires the radial component of the magnetic field in the photosphere, and therefore is less affected by errors in transverse field measurement. Using an improved version of this method, Bobra et al. (2008) constructed NLFFF models for two active

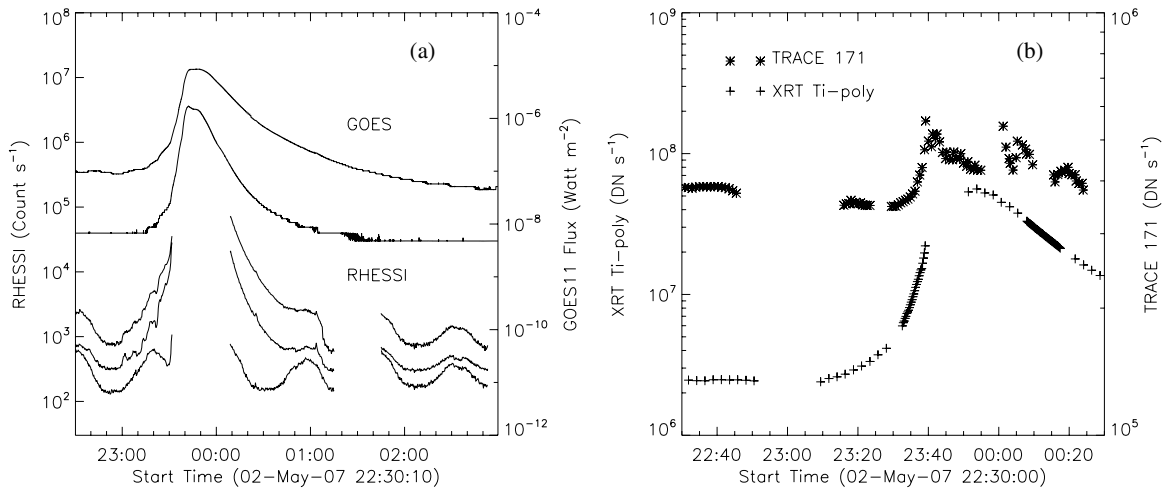


**Figure 1.** Light curves for the C8.5 two-ribbon flare occurred on 2007 May 2. The top two curves in the left panel refer to the *GOES* soft X-ray light curves at 1.0–8.0 Å and 0.5–4.0 Å while the bottom three, from top to bottom, refer to *RHESSI* X-ray light curves at 3–6 keV, 6–12 keV, and 12–25 keV, respectively. The *RHESSI* light curve at 3–6 keV is multiplied by 4 in order to give a nicer display. *TRACE* EUV and *XRT* X-ray light curves are marked by star sign and plus sign on the right panel, respectively.

regions based on magnetograms from the Michelson Doppler Images (MDI) aboard *SOHO* and nonpotential structures seen in *TRACE* EUV images. They found that *TRACE* images are not well suited to the task of finding sheared fields near polarity inversion lines (PILs). Therefore, in the current paper multiple nonpotential X-ray loops observed by *Hinode*/*XRT* are used to constrain the models. We also use vector magnetograms from *Hinode*/SOT/SP to derive the radial field in the photosphere. This allows us to correct for the fact that the observed AR is about 15° away from the disk center.

This paper is organized as follows. Section 2 describes the observations, and Section 3 describes how the NLFFF models are constructed and the modeling results. The discussion and interpretation are given in Section 4. Conclusions are presented in Section 5.

## 2. OBSERVATIONS

### 2.1. Data Sets and Instruments

NOAA Active Region (AR) 10953 is a simple bipolar active region, which produced several filament activations and small flares (< M class) in 2007 May. A long-term movie of the *SOHO*/MDI magnetograms shows that the leading sunspot in this active region is a decaying sunspot, which ejected numerous magnetic elements toward the polarity inversion line, where flux cancellations frequently occurred.

A C8.5 (*GOES* soft X-ray class) two-ribbon flare associated with a filament activation occurred in AR 10953 around 23:20 UT on 2007 May 02. This event was well observed in multiple wavelengths, i.e., soft X-rays by the X-ray Telescope (*XRT*; Golub et al. 2007) onboard *Hinode* (Kosugi et al. 2007), EUV by the *Transition Region and Coronal Explorer* (*TRACE*; Handy et al. 1999), and H $\alpha$  by the Polarimeter for Inner Coronal Studies (PICS) which has been operated by the High Altitude Observatory at the Mauna Loa Solar Observatory (MLSO) since 1994. This flare was also observed by *RHESSI* (Lin et al. 2002) except the two gaps caused by the night time of the spacecraft. The full disk H $\alpha$  images ( $\sim 1''.09$  pixel $^{-1}$ ) taken at the Kanzelhöhe Solar Observatory (KSO) are also used. The *XRT* images presented in this study are taken with the Ti-poly filter and have field of view (FOV) of 512'' $\times$ 512''. The spatial resolution is around 2'' (1''.032 pixel $^{-1}$ ). The *TRACE* EUV images

are taken at 171 Å with an FOV of 1024'' $\times$ 1024'', and the spatial resolution is 1''. The full disk H $\alpha$  images taken by PICS with 3 minute cadence have a spatial resolution of 2''.9. The X-ray light curves of this event are provided by *GOES* and *RHESSI*.

The magnetic field information is obtained from the line-of-sight photospheric magnetograms from *SOHO*/MDI and vector magnetogram from the Spectro-Polarimeter (SP) of the Solar Optical Telescope (SOT; Tsuneta et al. 2008) onboard *Hinode*. The *Hinode* SP data were calibrated with the standard “SP\_PREP” software. The calibrated Stokes spectra were then subjected to the Milne–Eddington inversion procedure developed for the HAO/Advanced Stokes Polarimeter (Skumanich & Lites 1987; Lites & Skumanich 1990; Lites et al. 1993) to derive the magnetic field vector, fill fractions, and thermodynamic parameters over the map. No inversion was attempted for regions of the map where the net line polarization did not exceed 0.4%. For those regions we assumed the field to be vertical and equal to the apparent flux density derived from the integrated Stokes V polarization signal. We then resolved the 180° azimuth ambiguity with the AZAM utility (Lites et al. 1995), which minimizes the spatial discontinuities in the azimuth angle when viewed in the local reference frame.

The *TRACE* and *XRT* images are co-aligned with the MDI magnetograms by applying the following procedures. We first determined the offset of the *TRACE* coordinates by aligning the *TRACE* WL images with the corresponding WL images taken by MDI using sunspots as references. The offset between the *XRT* and *TRACE* images with corrected coordinates is determined by aligning the brightenings (i.e., flare footpoints) in the *TRACE* EUV images and the corresponding *XRT* images. We aligned the H $\alpha$  images from the PICS and KSO with the MDI magnetograms by eye.

The *XRT* images prior to the C8.5 flare show a number of highly sheared loops that indicate the presence of a coronal flux rope or highly sheared arcade above the PIL of the AR. These loops will be described in Section 3.2, where we use these loops to construct nonpotential field models of the AR.

### 2.2. Pre-EUV Flare X-ray Brightenings

The *GOES* (top two) and *RHESSI* (bottom three) X-ray light curves for the C8.5 two-ribbon flare are shown in Figure 1(a).

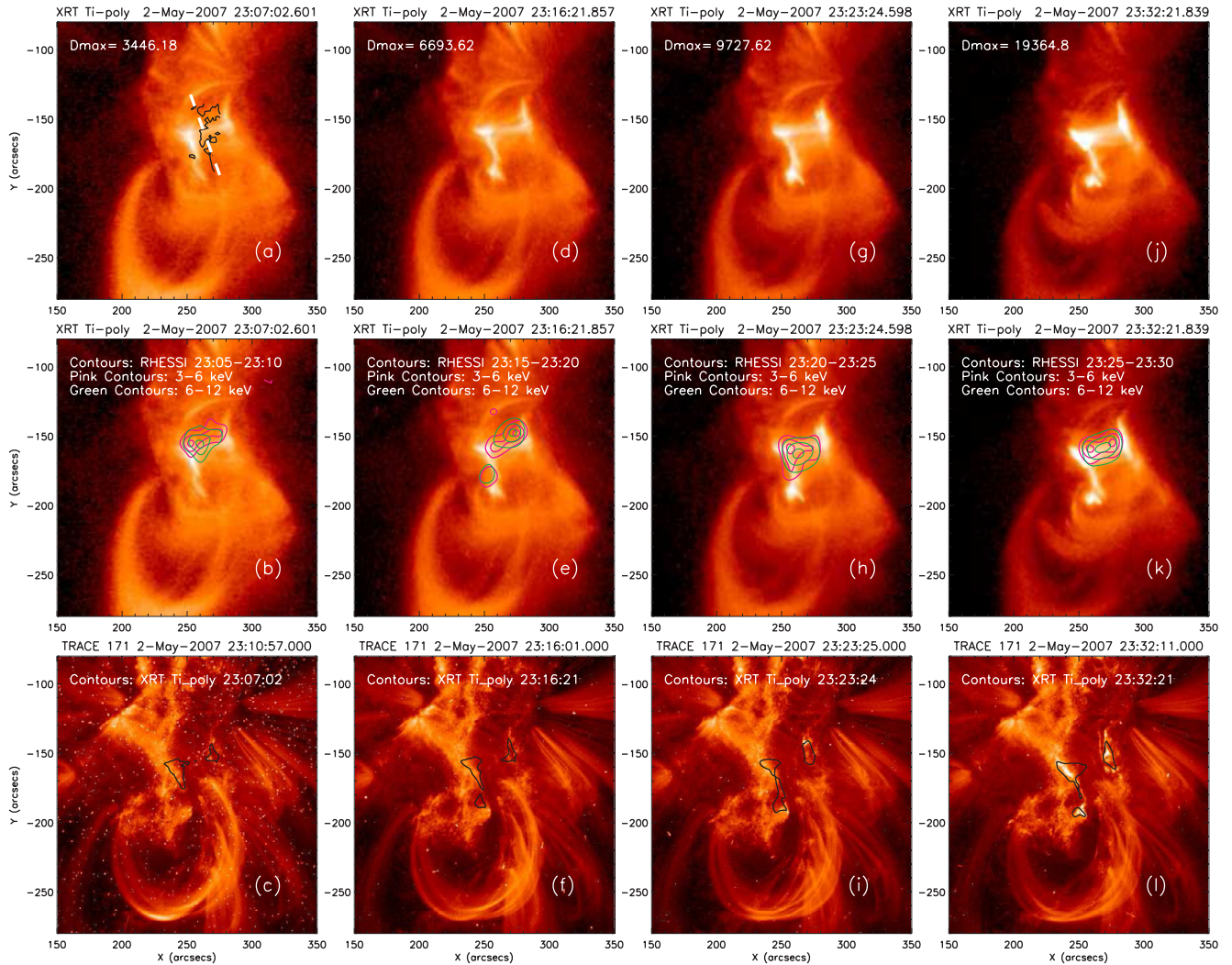


**Figure 2.** Pre-EUV X-ray brightenings during the C8.5 flare. The background images in the top and middle panels show the XRT observations at the early phase of the C8.5 flare. The XRT data are plotted in logarithm scale, and the maximum intensity ( $D_{\max}$ ,  $\text{DN s}^{-1}$ ) of the XRT images is shown on the top of each panel. The white line in panel (a) refers to the polarity inversion line obtained from MDI magnetogram, and the black dashed line is a simplified PIL corresponding to the  $H\alpha$  filament. The white and gray contours overlaid on the middle panels refer to 3–6 keV and 6–12 keV *RHESSI* observations, respectively. The X-ray contours (XRT) overlaid on the corresponding *TRACE* EUV images are shown in the bottom panels.

(A color version of this figure is available in the online journal.)

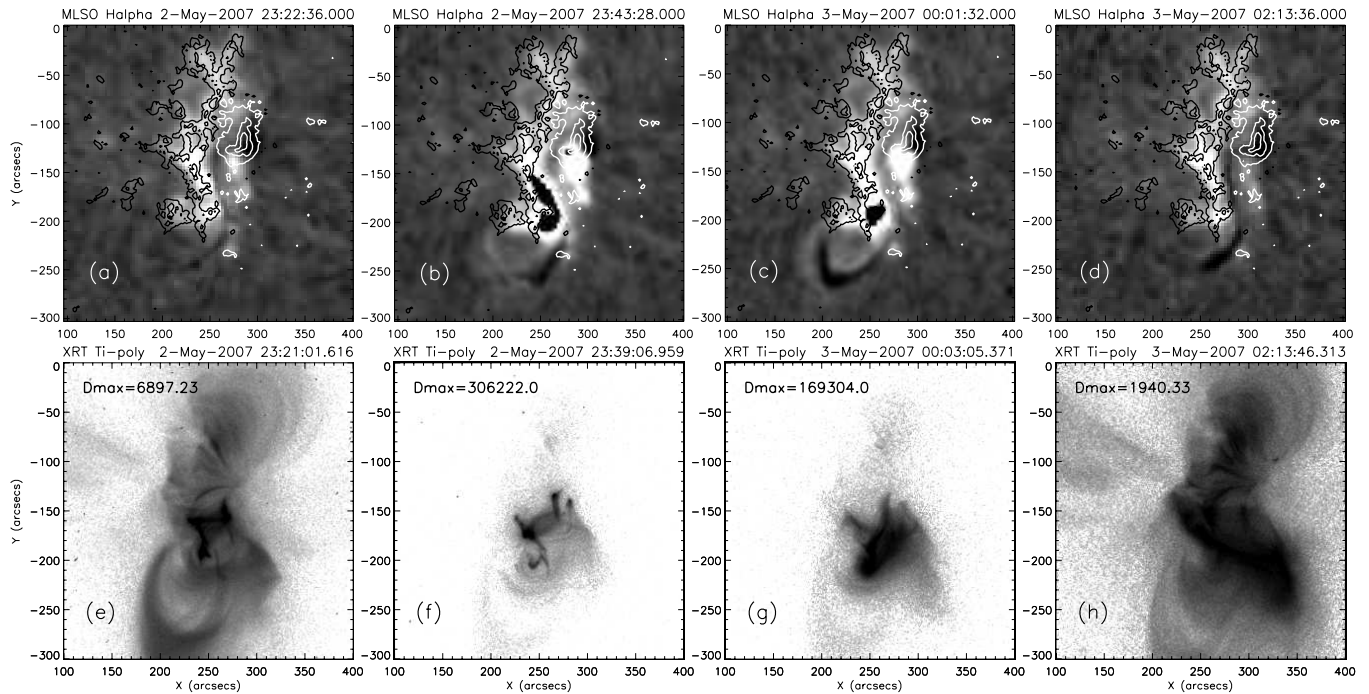
The two gaps in *RHESSI* light curves are during its night times. *GOES* light curves show that the flare started around 23:12 UT and peaked at 23:48 UT on 2007 May 2, and ended about 02:00 UT on 2007 May 3. Small spikes started to be seen after 23:00 UT in the lower energy band (3–6 keV and 6–12 keV) of *RHESSI* light curves. The higher energy band (12–25 keV) was dominated by the background most of the time, and a real increase in the light curve started around 23:30 UT. Figure 1(b) shows the integrated light curve of the flare region (as shown in Figure 2) in *TRACE* EUV and XRT X-rays. The first gap in the *TRACE* light curve is a real observational data gap. We also removed the images with strong particle hits, which lead to the other three gaps in the *TRACE* light curve. The images during the first gap in the XRT light curve were affected by strong atmospheric absorption. The images during the other gaps of the XRT light curve are saturated. From this figure we see that the soft X-ray light curve began to rise around 23:10 UT (similar to *GOES*), while the EUV flare started about 20 minutes later.

Figure 2 shows the XRT, *RHESSI*, and *TRACE* EUV images at the early phase of the C8.5 flare. The XRT data used in this figure are normalized to its maximum value ( $D_{\max}$ , in unit of  $\text{DN s}^{-1}$ ),

which is presented in the top of each panel. At 23:07 UT, XRT started to see two short ribbon-like brightenings connected by a loop that is nearly perpendicular to the underlying PIL (black and white lines in Figure 2(a)). Corresponding X-ray sources are seen in *RHESSI* observations in its lowest energy band (see Figure 2(b)). There are no counterparts of the X-ray brightenings in the EUV image as seen from Figure 2(c). A similar result is obtained from the observations at 23:16 UT and 23:23 UT (the middle two columns of Figure 2). A filament activation began around 23:20 UT, after which a rapid increase is seen in the *GOES* light curve, and tiny EUV footprint brightenings became visible (Figure 2i). However, the EUV brightenings are much smaller than the corresponding X-ray brightenings at this time. Several minutes later, most of the EUV counterparts of the X-ray brightenings can be seen in the *TRACE* images (Figures 2l).

### 2.3. Evolution of the Filament Activation

The evolution of the filament activation associated with the C8.5 flare in  $H\alpha$  (MLSO/PICS) is shown in the top panels of



**Figure 3.** Evolution of the filament activation associated with the C8.5 flare. The top panels show the MLSO/PICS  $H\alpha$  observations of this filament activation. The white and black contours refer to the negative and positive magnetic fields observed by *SOHO*/MDI. The corresponding closest in time *Hinode*/XRT images are shown in the bottom panels. The evolution of this filament activation (in  $H\alpha$ , *TRACE* EUV, and XRT) is also available as a video in the electronic edition of the *Astrophysical Journal*.

Figure 3. The  $H\alpha$  image at the onset of the filament activation is displayed in Figure 3(a), which shows that the northern end of the filament is rooted in the leading sunspot with negative polarity (*white contours*), but the southern end of this filament is unclear. This southern end of the filament is very unstable, and many activations were observed at multiple wavelengths (i.e.,  $H\alpha$ , EUV, and X-ray) from April 30 to May 3. After 23:20 UT, a large amount of filament material moved from the northern part of the filament to the southern part (Figure 3(b)), then streamed into the nearby positive polarity region (Figure 3(c)). This filament activation was also seen in *TRACE* EUV observations (see online video), while no clear evidence is seen in the X-ray images as shown in the bottom panels of Figure 3. Figure 3(d) shows an  $H\alpha$  image at about three hours after the onset of the filament activation. A comparison of Figures 3(a) and 3(d) shows that the shapes of the filament before and after the activation are very similar, but the  $H\alpha$  filament after the activation appears to be darker than before.

### 3. NLFFF MODELING

#### 3.1. Flux Rope Insertion Method

A flux rope insertion method has been developed by van Ballegoijen (2004) and van Ballegoijen & Mackay (2007) for constructing NLFFF models of solar active regions and filaments. In this paper, we use an improved version of this method; a detailed description can be found in Bobra et al. (2008). The method involves inserting a magnetic flux rope into a potential-field model of an active region; the axial flux  $\Phi_{\text{axi}}$  and poloidal flux  $F_{\text{pol}}$  of the flux rope are treated as free parameters. Magnetofrictional relaxation is applied by solving the MHD induction equation, including the effects of magnetic diffusion (see equation A2 in Bobra et al. 2008). The computation is done on a 3D grid in spherical coordinates with the lower boundary located at the photosphere. At the lower

boundary of the computation domain only the *radial* component  $B_r$  of the magnetic field needs to be specified; the tangential components  $B_\theta$  and  $B_\phi$  are allowed to vary in the relaxation process. The parameters  $\Phi_{\text{axi}}$  and  $F_{\text{pol}}$  are estimated by comparing the modeled field lines with observed  $H\alpha$  filaments and coronal loops.

The use of magnetic diffusion in NLFFF relaxation was investigated by Roumeliotis (1996), who used resistive diffusion in order to change the magnetic topology of the modeled field. The resistivity was assumed to be proportional to the magnitude of the Lorentz force,  $\eta \sim |\mathbf{j} \times \mathbf{B}|$ , where  $\mathbf{B}$  is the magnetic field and  $\mathbf{j}$  is the electric current density. The advantage of this approach is that diffusion occurs only in the unrelaxed state far from force-free equilibrium, not in the relaxed state when  $|\mathbf{j} \times \mathbf{B}|$  is almost zero. However, in the present case, we want to preserve the magnetic topology of the flux rope as best as possible. Ordinary (resistive) diffusion does not conserve magnetic helicity (Berger 1984), so significant changes in topology can occur during the relaxation process. In the present work, we use *hyperdiffusion*, which is a type of magnetic diffusion that conserves magnetic helicity and is described by a fourth-order diffusion operator (see van Ballegoijen & Cranmer 2008, and references therein). The advantage of hyperdiffusion in the present application is that it acts to suppress small-scale numerical artifacts in the electric current distribution without significantly affecting the large-scale electric currents. Therefore, the topology of the magnetic field is nearly conserved during the relaxation process.

In this paper, we apply the flux rope insertion method to AR 10593 as observed on 2007 May 2 at 17:30 UT. The radial field  $B_r$  in the central part of the AR was derived from a photospheric vector magnetogram obtained with SOT/SP. The observed vector field was rotated to the local reference frame and remapped onto the longitude–latitude grid at the base of the 3D model. This grid has a heliocentric angular

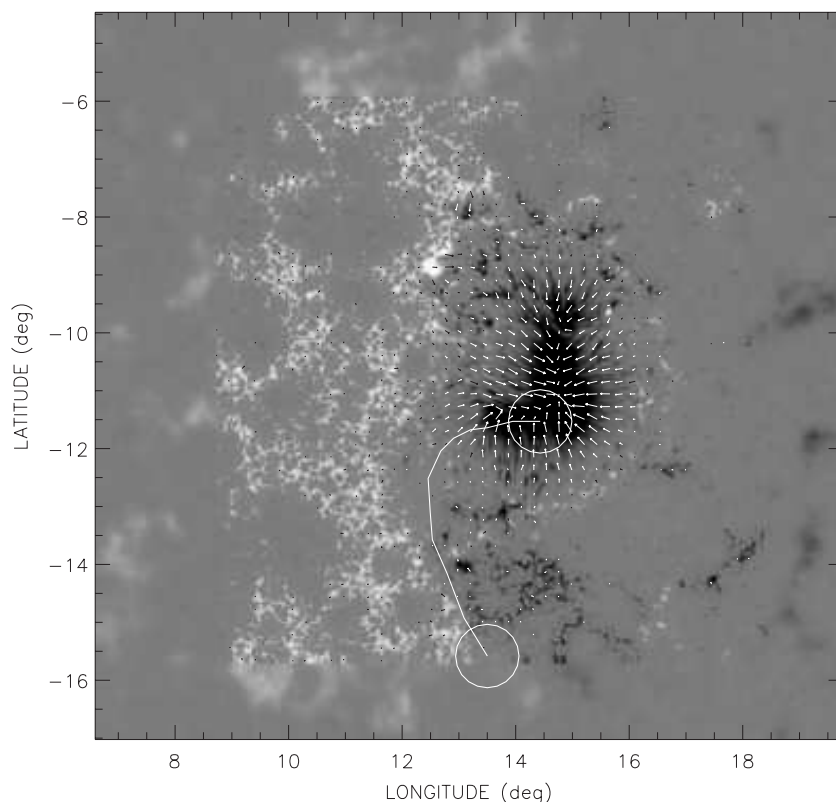


**Figure 4.** Magnetic map of AR 10953 on 2007 May 2 at 17:30 UT derived from *Hinode*/SOT/SP and *SOHO*/MDI data. The grayscale image shows the radial magnetic field  $B_r$  in the photosphere as function of longitude and latitude on the Sun (white for  $B_r > 0$ , black for  $B_r < 0$ ). The strongest field strength in the sunspot umbra is  $-2958$  G. The vectors show the horizontal components of the observed magnetic field. The vectors are plotted in black or white depending on whether the background is light or dark, and very short vectors are omitted from the plot. The white line ending with two circles refers to the selected filament path along which the flux rope is inserted.

resolution of  $0.00065 \cos \lambda$  radians, where  $\lambda$  is the latitude (for details see Bobra et al. 2008). In the areas outside the SOT/SP field of view, we estimated  $B_r$  from lower resolution *SOHO*/MDI magnetograms, assuming the field is nearly radial. Figure 4 shows the radial field as function of longitude and latitude. The vectors show the observed vector field in the local reference frame. The white line ending with two circles refers to the selected filament path along which the flux rope is inserted.

### 3.2. Modeling Results

For AR 10953 at 17:30 UT, we constructed a potential field model and a grid of NLFFF models with different values of axial and poloidal fluxes of the flux rope. Some of the models we constructed converge to a NLFFF equilibrium state, while others do not converge and the flux ropes lift off. Such “lift-off” occurs when the overlying coronal arcade is unable to hold down the flux rope in an equilibrium state, which happens when the axial and/or poloidal fluxes exceed certain limits. This lift-off is a result of the “loss of equilibrium” of the magnetic system, and is not a numerical problem. Therefore, stable NLFFF exists only when axial and poloidal fluxes are below certain limits.

The time of 17:30 UT is about 2.5 hr prior to a B3.8 flare (see Reeves et al. 2008) and 7.5 hr before the C8.5 flare. We determine the best model for AR 10953 based on the following two criteria: (1) this model should best fit the observed highly sheared X-ray loops; and (2) this model should converge to a stable solution.

#### 3.2.1. Comparisons with X-ray Loops

To constrain the model, we select four nonpotential X-ray loops that appeared in the XRT images at various times. The loops are numbered 1 to 4, and are shown in the four columns of Figure 5. These loops are marked by white and black arrows in the top panels and represented by red lines in the bottom panels. Loop 1 shows a clear S-shaped structure, which first appeared in the XRT observations around 11:00 UT on May 2. Loop 2 is a long and highly sheared loop, and showed up in XRT observations at 15:07 UT on May 2. Both Loop 1 and Loop 2 vanished in association with a partial filament eruption after 16:30 UT. Loop 3 appeared around 22:31 UT and was visible in XRT images until the C8.5 flare began ( $\sim 23:11$  UT). Loop 4 appeared after the filament eruption around 17:40 UT and disappeared around 19:20 UT. Moreover, the shape of Loop 4 is continuously evolving since its appearance in XRT. The blue and light blue lines refer to those model field lines that best fit the observed X-ray loops. These modeled field lines are from different models, and the poloidal flux (Pol) and axial flux (Axi) of the flux rope in these models are displayed in each panel. This figure indicates that our best-fit NLFFF models show very good fit to the observed sheared X-ray loops.

In order to find the model that best fits the observations of a particular loop, we use the following procedure. We define the “average deviation” (AD) between an observed loop and a modeled field line by measuring the distance between a point on the observed loop and the closest point on the projected field line in the image plane, and then averaging these distances for various points along the observed loop. This AD is in unit of solar radii. For each model we manually select the field

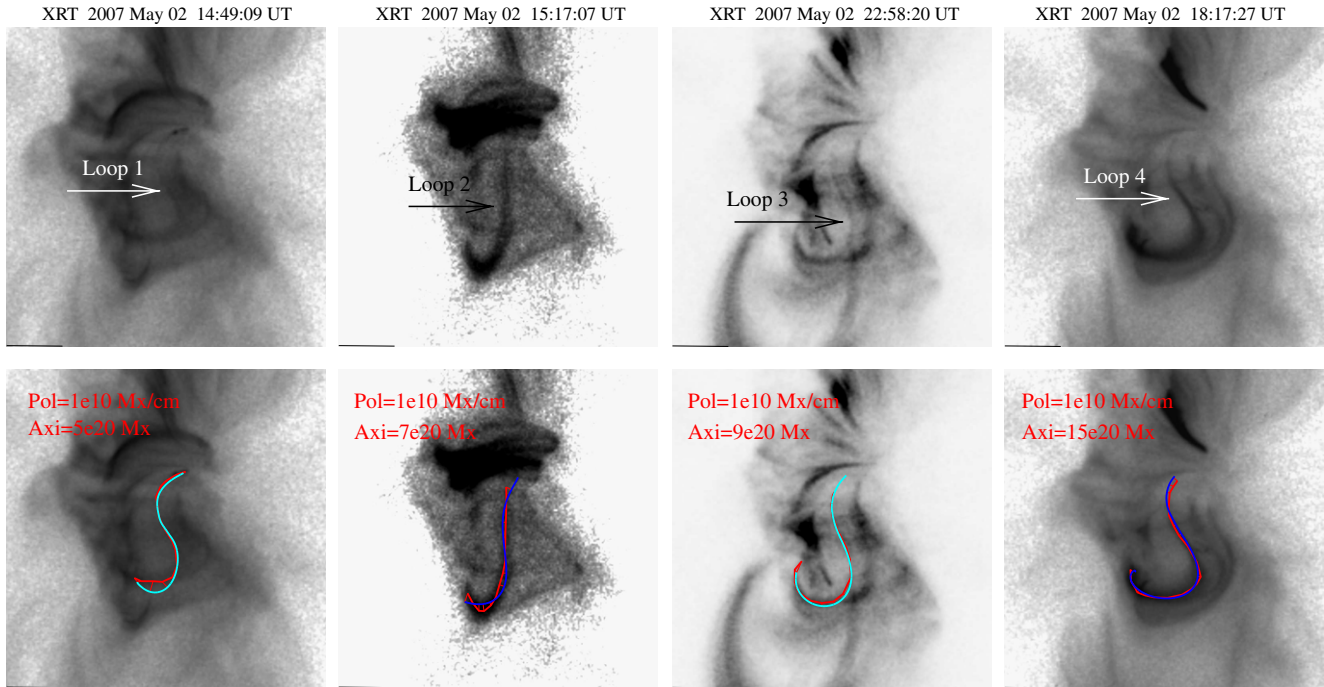


**Figure 5.** NLFFF models with different axial flux for AR 10953 vs. the observed nonpotential X-ray loops on 2007 May 2. The top panels show the four X-ray loops observed at different times prior to the C8.5 flare. The same loops (red line) overlaid with the best-fit model field lines (blue, light blue) are shown in the bottom panels. The axial and poloidal fluxes of each model are written on the upper part of each panel. The FOV of each panel is  $0.2 R_{\odot}$ .

line that can minimize this AD; this is the 3D field line that best fits the observed coronal loop. Table 1 summarizes the ADs of the best-fit modeled field lines from the observed X-ray loops for various models of AR 10953. The left two columns of Table 1 show the loop number and poloidal flux ( $F_{\text{pol}}$ ) of the model, and models with different axial flux ( $\Phi_{\text{axi}}$ ) are listed in the other columns. Table 1 is composed of four main rows, corresponding to different X-ray loops. The three rows of the first main row show the ADs of modeled field lines from Loop 1 for models with different  $F_{\text{pol}}$ . Similar information for Loops 2, 3, and 4 are shown in the second, third, and last main rows. The ADs for the models that are marginally stable are marked with underline in Table 1. Here “marginally stable” indicates that after 30,000 iterations of relaxation it is still unclear whether the model is stable or not. The ADs for the models which do not converge and the flux ropes lifting off are marked with double underlines in Table 1.

From Table 1 we can see that the models with axial flux of  $5 \times 10^{20}$  Mx,  $7 \times 10^{20}$  Mx,  $9 \times 10^{20}$  Mx, and  $12 \times 10^{20}$  Mx are the best-fit models for Loop 1, Loop 2, Loop 3, and Loop 4, respectively. The ADs of the best-fit models are written in italics. We also found that the best-fit model for Loop 4 is marginally stable, which is consistent with the XRT observations of continuous evolution of Loop 4. Therefore, the result for Loop 4 will not be considered to determine the best-fit model for AR 10953. The comparisons with Loops 1, 2, and 3 indicate that the best-fit model for AR 10953 has an axial flux of  $(7 \pm 2) \times 10^{20}$  Mx. Table 1 also shows that the poloidal flux in the best-fit models is  $1 \times 10^{10}$  Mx. However, for most models, the difference between the ADs of the models with different order of magnitudes of poloidal flux are often within the error bars. This indicates that the poloidal flux of the best-fit model has a much wider range, i.e., the XRT observations do not provide strong constraints on the poloidal flux. Table 1 also shows that the upper limit on the axial flux for stable force-free configurations is  $15 \times 10^{20}$  Mx.

**Table 1**  
AD of the Model Field Lines from the Observed X-ray Loops for Various Models of AR 10953 at 17:30 UT on 2007 May 2

Loop	$F_{\text{pol}} (10^{10} \text{ Mx cm}^{-1})$	$\Phi_{\text{axi}} (10^{20} \text{ Mx})$				
		5	7	9	12	15
		AD $\pm 0.2 (10^{-3} R_{\text{sun}})$				
Loop 1	0.1		2.8	3.2	5.3	
	1	<i>1.7</i>	2.0	2.5	3.1	<u>5.6</u>
	10		2.7	2.8	3.4	
Loop 2	0.1		2.2	2.4	2.6	
	1	3.5	2.2	2.4	2.6	<u>3.1</u>
	10		3.7	2.4	<u>2.7</u>	
Loop 3	0.1		1.9	1.3	1.7	
	1	3.9	1.8	<i>1.3</i>	1.8	<u>2.4</u>
	10		3.7	1.8	<u>1.9</u>	
Loop 4	0.1		4.4	3.2	2.0	
	1	6.7	4.7	3.4	2.0	<u>1.2</u>
	10		5.8	5.3	<u>3.8</u>	

### 3.2.2. Comparisons with Observed Vector Fields

Figure 6 shows a comparison of modeled horizontal field (black arrows) and the horizontal field derived from the SOT/SP observations (blue arrows). This figure shows only a small region of the Southeastern quadrant of the sunspot penumbra (see Figure 4). This is where the largest deviations from the potential field model occur. Figure 6(a) shows the potential field, while Figures 6(b)–6(d) show NLFFF models with fixed poloidal flux but different axial flux, which are marked on the top of each panel. From Figure 6 we can see that all of the three NLFFF models show much better fit to the observations than the potential field model. The error of the azimuth angle (i.e., the average angle between the modeled and observed vectors) weighted by the square of the observed

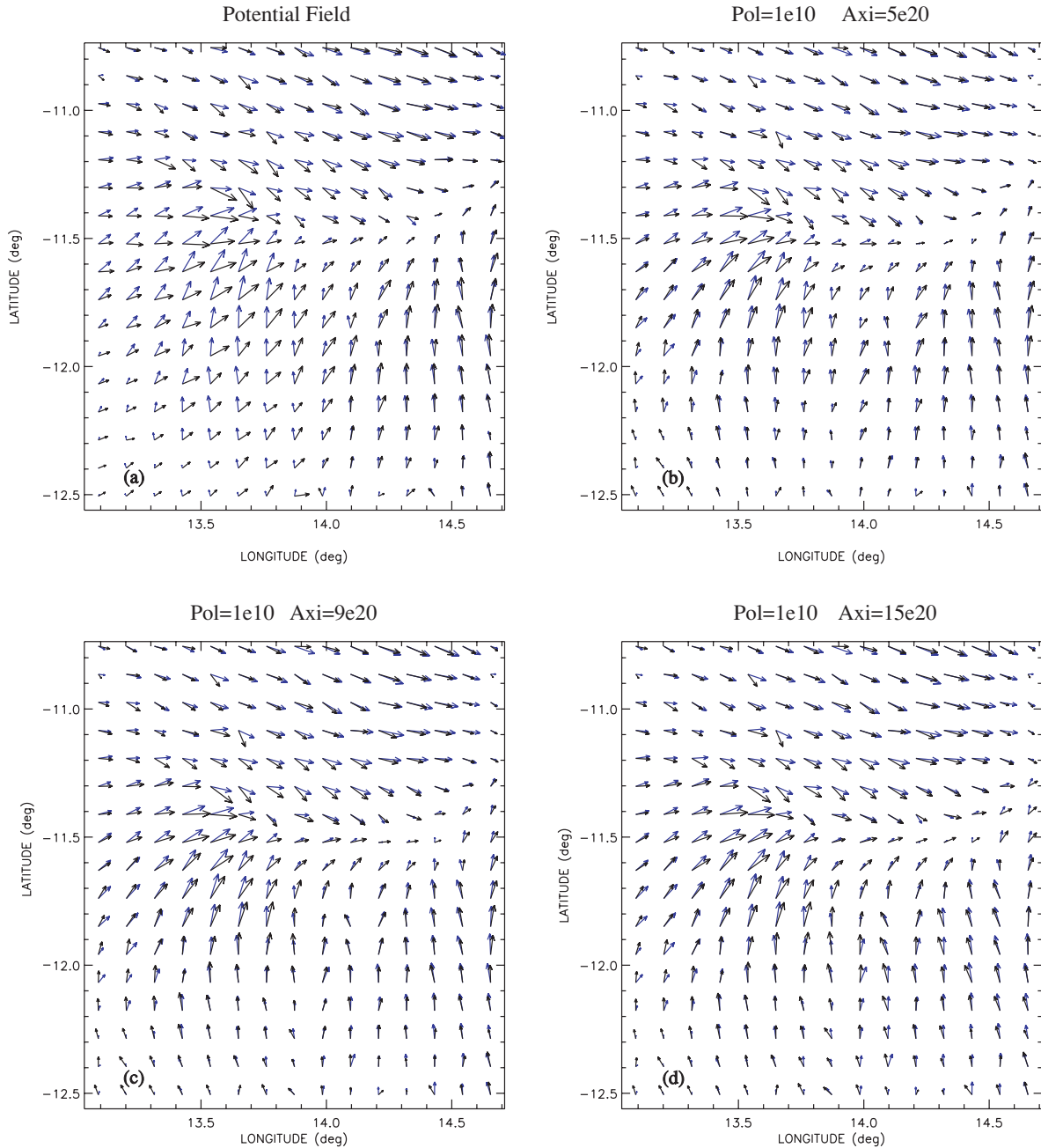


**Figure 6.** Comparison of observed (blue, SOT/SP) and modeled (black) vector magnetograms. The FOV of each panel is marked by a white box in Figure 4. The model in panel (a) is a potential field model, while the models in panels (b)–(d) are three NLFFF models with fixed poloidal flux but different axial flux, which are written on the top of each panel.

horizontal field in each panel has been calculated. The azimuth errors in Figures 6(a)–6(d) are  $26^{\circ}10'$ ,  $15^{\circ}73'$ ,  $13^{\circ}88'$ , and  $13^{\circ}82'$ , respectively. This result appears to suggest that the NLFFF model with higher axial flux fits the observed vector fields better, but the differences between the azimuth errors for the three NLFFF models are not significant. The azimuth errors are much larger than the measurement errors. Therefore, the present models do not provide an accurate fit to the vector field data.

#### 4. DISCUSSION AND INTERPRETATION

Figure 7 shows the results of one of the best-fit models for Active Region 10953 at 17:30 UT. The blue lines in

Figures 7(a)–7(b) are selected model field lines within the flux rope that best fit the observed X-ray Loops 1, 2, and 3. Figure 7(c) shows the distribution of the radial electric current density  $j_r$  at a height of 6.3 Mm above the photosphere; the currents flow upward on the eastern side of the flux rope ( $j_r > 0$ ) and downward on the western side ( $j_r < 0$ ). Figure 7(d) shows a vertical cross section of the flux rope along the yellow line shown in Figure 7(c); the center of the flux rope is located at  $s = 30$ ,  $z = 15$  (cell units). The grayscale image in Figure 7(d) shows the component of the current density parallel to the flux rope. The circular white region shows that the currents are concentrated at the edge of the flux rope, i.e., they have a *hollow core* distribution. In the gray central part of the flux rope the field lines are parallel to the PIL, and therefore highly

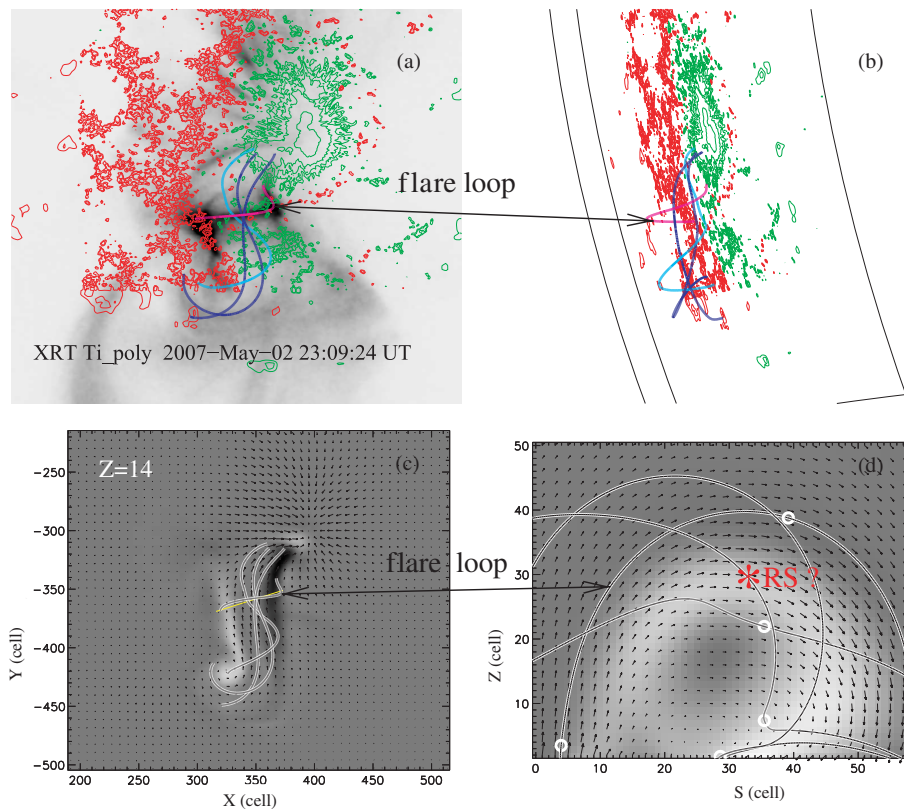


**Figure 7.** Results for one of the best-fit NLFFF model ( $\text{Pol}=1e10 \text{ Mx/cm}$ ,  $\text{Axi}=9e20 \text{ Mx}$ ) for Active Region 10953 at 17:30 UT on 2007 May 2. (a) XRT image at the flare onset overlaid with red and green contours representing positive and negative polarities. (b) A side view of (a). The FOV of (a) and (b) is  $0.2 R_{\odot}$ . (c) Distribution of radial component of current density,  $j_r(x, y, 14)$ . (d) Hollow core distribution of electric currents in a vertical cross section of the flux rope. The location of the vertical plane is shown by the yellow line in panel (c). The white region refers to the current layer, and a possible RS at the flare onset is marked by a red star. The white circles represent the crossing point of the model field lines and the yellow line in panel (c). The color lines in panels (a) and (b) and the white lines in panels (c) and (d) refer to the selected model field lines. The field line marked by black arrows refer to one of the best-fit model field lines for a nearly potential flare loop, which appears at the flare onset.

sheared compared to the potential field, but nearly untwisted because there is no current in this region. In the white region the direction of the magnetic field changes from parallel to the PIL on the inside of the flux rope to perpendicular to the PIL on the outside. The coronal arcade overlying the flux rope is close to a potential field.

The pink line in Figures 7(a)–7(b) is the modeled field line that best fits the nearly unsheared X-ray loop observed at the onset of the C8.5 flare. The side view in Figure 7(b) indicates that this pink line overlies the other three field lines. Figure 7(d) shows that this field line is located just beyond the outer edge of the flux rope where the magnetic field is nearly unsheared and the current density is small. Therefore, the observation of an unsheared loop so close to the flux rope confirms that the magnetic shear falls off rapidly with distance from the outer edge of the flux rope, as assumed in the present model. We conclude that the electric currents in AR 10953 are concentrated in a relatively thin shell at the outer edge of the flux rope, not on the flux rope axis. A similar result was found by Bobra et al. (2008) for two other active regions.

Su et al. (2007a) classified flares according to the degree of shear of the flare footpoints. They showed that for most Type I (ejective) flares the initial flare brightenings are highly sheared with respect to the PIL, indicating that the reconnection site (RS) responsible for particle acceleration and heating initially lies somewhere inside the highly sheared magnetic field. Later during the flare the shear angle usually decreases. In contrast, Type II (confined) flares do not have highly sheared footpoint

brightenings, and have no obvious shear change during the flare. The C8.5 flare considered here appears to start as a Type II flare because the X-ray loop observed at flare onset is nearly unsheared and apparently located just beyond the outer edge of the flux rope.

The fact that the observed X-ray loop is located *outside* the flux rope suggests that the flux rope is initially not the main source of energy for the flare. Su et al. (2007a) discussed three possible models for the initiation of Type II flares: emerging (or evolving) flux model; (resistive) kink instability; and confined explosion of a sheared bipole. In the last case one would expect that the reconnection first occurs inside or below the flux rope (Moore et al. 2001). Then the newly reconnected loop should be highly sheared and close to the PIL, which is contrary to our observations of the C8.5 flare. We also did not find any evidence to support the (resistive) kink instability model. Therefore, we focus our attention on the emerging or evolving flux model. This model was first proposed by Heyvaerts et al. (1977), who suggested that solar flares occur when loops of flux emerge from below the photosphere and interact with the overlying field. During the preflare heating phase, continuous reconnection occurs in the current sheets that forms between the new and old flux. Waves that radiate from the ends of the current sheet heat the plasma that passes through them and causes an increase in soft X-ray emission. This model has been generalized to give an Interacting Flux Model with either vertically emerging flux or horizontal spot motions (Priest & Forbes 2002). Interacting flux can show up in many ways, such as the motion of pores

(Raadu et al. 1988), of emerging flux (Simon et al. 1984; Rust et al. 1994) and of cancelling magnetic features (Martin et al. 1985; Wang & Shi 1993).

No large-scale flux emergence was evident in AR 10953 in a long-term movie of MDI magnetograms (May 1 to May 3). However, many moving magnetic features can be seen around the sunspot, and cancelling features are present near the PIL. Therefore, we speculate that at the flare onset magnetic reconnection occurred between two or more loops located somewhere near the outer edge of the flux rope (a possible RS is marked as a red star in Figure 7(d)), resulting in the direct heating of the observed X-ray loop. Although only one X-ray loop is visible in XRT at this stage, we suggest that the observed feature may consist of multiple reconnected (and heated) loops, or that one of the newly formed loops is denser than the others. Initially the flare involved only the magnetic field of these reconnecting loops, but after about 10 or 20 minutes the reconnection spread to the outer parts of the flux rope, triggering the release of a much larger amount of energy stored in the flux rope. Therefore, the main phase of the flare involved reconnection inside the flux rope. This scenario is consistent with the fact that during the main phase of the flare the EUV footpoint brightenings are highly sheared, as expected for reconnection occurring in a highly sheared magnetic field. In summary, we suggest that the initial phase of the C8.5 flare may have been caused by interactions of weakly sheared loops near the outer edge of the flux rope, but during the main phase of the flare the reconnection involved the inner parts of the flux rope, which are highly sheared.

As shown in Section 2.2, the X-ray brightenings (in both *RHESSI* and XRT) appeared about 20 minutes earlier than the *TRACE* EUV flare brightenings, which showed up associated with a filament activation. XRT observations show that these early X-ray brightenings appear to be two bright short ribbons connected with a nearly potential loop, i.e., a loop that follows more or less the direction of the potential magnetic field. The *RHESSI* spectral fitting suggests that the pre-EUV X-ray sources are dominated by thermal emission from an isothermal hot plasma with a temperature higher than 10 MK. This result is consistent with the absence of detectable hard X-ray emission ( $> 25$  keV) prior to the onset of the EUV flare.

It is known that there are mainly two kinds of mechanisms for the EUV footpoint brightenings: thermal conduction from the reconnected loops, and direct bombardment of the lower atmosphere by accelerated particles from the RS (Fletcher & Hudson 2001). The second EUV brightening mechanism can be excluded at the early phase of this flare, because of the absence of accelerated particles indicated by the X-ray observations. However, the hot X-ray sources suggest that there are direct heating in the lower corona probably due to reconnection. The question is why no EUV brightenings were observed corresponding to the long-lasting ( $\sim 20$  minutes) hot X-ray sources? One possibility is that at the pre-EUV X-ray flare phase, the thermal conduction from the corona was suppressed due to some unknown reasons, plus the energy released at this phase is also very low. Therefore, almost no energy was propagated to the chromosphere through thermal conduction to produce EUV brightenings.

## 5. CONCLUSIONS

Using the flux rope insertion method, we constructed a series of NLFFF models for AR 10953 prior to a B3.8 and a C8.5 flare on 2007 May 2. The models are created mainly based on the radial field derived from magnetograph data provided by

*Hinode*/SOT/SP and *SOHO* MDI, and an H $\alpha$  filament observed by KSO. By comparisons with four X-ray loops observed by *Hinode*/XRT, we find that the axial flux of the flux rope in the model is well constrained by Loops 1, 2, and 3, while Loop 4 may be in a nonstable state.

By comparisons with the observed X-ray loops, we find that the axial flux of the flux rope in the best-fit model is  $(7 \pm 2) \times 10^{20}$  Mx, while the poloidal flux has a wider range, i.e.,  $(0.1-10) \times 10^{10}$  Mx cm $^{-1}$ . The axial flux in the best-fit model is well below the upper limit ( $\sim 15 \times 10^{20}$  Mx) for stable force-free configurations, which is consistent with the fact that no successful full filament eruption occurred in this active region. The magnetic free energy in one ( $\Phi_{\text{axi}} = 7 \times 10^{20}$  Mx,  $F_{\text{pol}} = 1 \times 10^{10}$  Mx cm $^{-1}$ ) of the best-fit models is  $8.5 \times 10^{31}$  erg, which is about 10% of the potential energy ( $9.6 \times 10^{32}$  erg). This amount of free energy is sufficient to power a B3.8 flare and a C8.5 flare.

The interior of the flux rope in the best-fit model is highly sheared and weakly twisted. The electric current is concentrated at the edge of the flux rope, not on the axis (i.e., the highly sheared field region). This *hollow core* distribution is a consequence of the fact that the flux rope in this model is only weakly twisted, which is consistent with the finding by Bobra et al. (2008).

By comparisons of observed and modeled photospheric vector magnetograms, we find that our NLFFF models show much better fit to the observed vector fields than the potential field model. However, the azimuth errors (i.e., the average angle between the modeled and observed vectors) in the NLFFF models are about  $15^\circ$ , which is large compared to the measurement errors. There is no significant difference in the goodness-of-fit to the observed vector fields for the NLFFF models that we constructed. This poor fit is not surprising, since our models are mainly constrained by the observed X-ray loops, and no attempts was made to fit the observed vector field. Our best-fit model matches the observed loops well, but not the observed vector field. The flux rope insertion method is quite unlike the other kind of methods (Schrijver et al. 2008), which construct NLFF fields by extrapolating observed photospheric vector fields into the corona. These methods are mainly constrained by the photospheric vector fields, and Schrijver et al. (2008) found that even the best-fit model provides a rather poor match to the observed coronal loops. Therefore, our future goal of NLFFF reconstructions should be combining these two type of methods, and to produce models that provide a good fit to both the observed photospheric fields and the coronal fields (X-ray loops).

Two interesting observations are found in the C8.5 flare. The first one is that this flare started from nearly unshaped brightenings and loop, unlike most two-ribbon flares which begin with highly sheared footpoint brightenings as shown in Su et al. (2007a). By comparing with our NLFFF model, we find that this early flare loop is located above but very close to the outer edge of the flux rope. This flare is interpreted in the context of the Interacting Flux Model (Priest & Forbes 2002). We suggest that this flare may start near the outer edge of the flux rope, not at the inner side or at the bottom as suggested in the standard two-ribbon flare model (e.g., Moore et al. 2001).

Another interesting observation is that the X-ray brightenings (in both *RHESSI* and XRT) appeared about 20 minutes earlier than the EUV brightenings, which showed up associated with a filament activation. Our analysis suggests that the soft X-ray emission may be caused by direct coronal heating due to

reconnection. The energy transported to the chromosphere may be too low to produce EUV brightenings.

We thank the referee for helpful suggestions to improve this paper. *Hinode* is a Japanese mission developed and launched by ISAS/JAXA, with NAOJ as domestic partner and NASA and STFC (UK) as international partners. It is operated by these agencies in co-operation with ESA and the NSC (Norway). The authors thank the team of *Hinode*/XRT, *Hinode*/SOT, *TRACE*, *RHESSI*, *SOHO* MDI, MLSO, KSO, and *GOES* for providing valuable data. Y.S. acknowledges Kathy K. Reeves for helpful discussions. U.S. members of the XRT team are supported by NASA contract NNM07AB07C to the Smithsonian Astrophysical Observatory (SAO). The *TRACE* analysis are supported at SAO by a contract from Lockheed Martin. Y.S. is also supported by the NSFC projects with 10773032 and 10833007. The NLFFF modeling work was supported by NASA/LWS grant NNG05GK32G.

## REFERENCES

- Berger, M. A. 1984, *Geophys. Astrophys. Fluid Dyn.*, **30**, 79
- Bleybel, A., Amari, T., van Driel-Gesztelyi, L., & Leka, K. D. 2002, *A&A*, **395**, 685
- Bobra, M. G., van Ballegoijen, A. A., & Deluca, E. E. 2008, *ApJ*, **672**, 1209
- Canfield, R. C., Hudson, H. S., & McKenzie, D. E. 1999, *Geophys. Res. Lett.*, **26**, 627
- Fletcher, L., & Hudson, H. 2001, *Sol. Phys.*, **204**, 69
- Golub, L., et al. 2007, *Sol. Phys.*, **243**, 63
- Handy, B. N., et al. 1999, *Sol. Phys.*, **187**, 229
- Heyvaerts, J., Priest, E. R., & Rust, D. M. 1977, *ApJ*, **216**, 123
- Ji, H., Wang, H., Liu, C., & Dennis, B. R. 2008, *ApJ*, **680**, 734
- Kosugi, T., et al. 2007, *Sol. Phys.*, **243**, 3
- Lin, R. P., et al. 2002, *Sol. Phys.*, **210**, 3
- Lites, B. W. 2005, *ApJ*, **622**, 1275
- Lites, B. W., Elmore, D. F., Seagraves, P., & Skumanich, A. 1993, *ApJ*, **418**, 928
- Lites, B. W., Low, B. C., Martínez Pillet, V., Seagraves, P., Skumanich, A., Frank, Z., Shine, R. A., & Tsuneta, S. 1995, *ApJ*, **446**, 877
- Lites, B. W., & Skumanich, A. 1990, *ApJ*, **348**, 747
- Martin, S. F., Livi, S. H. B., & Wang, J. 1985, *Aust. J. Phys.*, **38**, 929
- McClymont, A. N., Jiao, L., & Mikic, Z. 1997, *Sol. Phys.*, **174**, 191
- Metcalf, T. R., et al. 2008, *Sol. Phys.*, **247**, 269
- Mikić, Z., & McClymont, A. N. 1994, in ASP Conf. Ser. 68, *Solar Active Region Evolution: Comparing Models with Observations* (San Francisco, CA: ASP), 225
- Moore, R. L., Sterling, A. C., Hudson, H. S., & Lemen, J. R. 2001, *ApJ*, **552**, 833
- Okamoto, T. J., et al. 2008, *ApJ*, **673**, L215
- Priest, E. R., & Forbes, T. G. 2002, *A&A Rev.*, **10**, 313
- Raadu, M. A., Schmieder, B., Mein, N., & Gesztelyi, L. 1988, *A&A*, **197**, 289
- Reeves, K. K., Seaton, D. B., & Forbes, T. G. 2008, *ApJ*, **675**, 686
- Régnier, S., Amari, T., & Kersalé, E. 2002, *A&A*, **392**, 1119
- Roumeliotis, G. 1996, *ApJ*, **473**, 1095
- Rust, D. M., & Kumar, A. 1996, *ApJ*, **464**, L199
- Rust, D. M., Sakurai, T., Gaizauskas, V., Hofmann, A., Martin, S. F., Priest, E. R., & Wang, J.-X. 1994, *Sol. Phys.*, **153**, 1
- Schrijver, C. J., et al. 2006, *Sol. Phys.*, **235**, 161
- Schrijver, C. J., et al. 2008, *ApJ*, **675**, 1637
- Simon, G., Mein, N., Mein, P., & Gesztelyi, L. 1984, *Sol. Phys.*, **93**, 325
- Skumanich, A., & Lites, B. W. 1987, *ApJ*, **322**, 473
- Song, M. T., Fang, C., Tang, Y. H., Wu, S. T., & Zhang, Y. A. 2006, *ApJ*, **649**, 1084
- Su, Y. N., Golub, L., & van Ballegoijen, A. A. 2007a, *ApJ*, **655**, 606
- Su, Y. N., Golub, L., van Ballegoijen, A. A., & Gros, M. 2006, *Sol. Phys.*, **236**, 325
- Su, Y. N., et al. 2007b, *PASJ*, **59**, S785
- Tsuneta, S., et al. 2008, *Sol. Phys.*, **249**, 167
- van Ballegoijen, A. A. 2004, *ApJ*, **612**, 519
- van Ballegoijen, A. A., & Cranmer, S. R. 2008, *ApJ*, **682**, 644
- van Ballegoijen, A. A., & Mackay, D. H. 2007, *ApJ*, **659**, 1713
- Wang, J., & Shi, Z. 1993, *Sol. Phys.*, **143**, 119
- Wheatland, M. S. 2006, *Sol. Phys.*, **238**, 29
- Wheatland, M. S., Sturrock, P. A., & Roumeliotis, G. 2000, *ApJ*, **540**, 1150
- Wiegelmann, T. 2004, *Sol. Phys.*, **219**, 87
- Wiegelmann, T. 2008, *J. Geophys. Res.*, **113**, A03S02
- Wiegelmann, T., Inhester, B., & Sakurai, T. 2006, *Sol. Phys.*, **233**, 215
- Yan, Y. H., & Sakurai, T. 2000, *Sol. Phys.*, **195**, 89